ARTICLE

doi:10.1038/nature10369

Crystal structure of nucleotide-free dynamin

Katja Faelber[1], York Posor[2]*, Song Gao[1,2]*, Martin Held[3]*, Yvette Roske[1]*, Dennis Schulze[1], Volker Haucke[2], Frank Noé[3] & Oliver Daumke[1,4]

Dynamin is a mechanochemical GTPase that oligomerizes around the neck of clathrin-coated pits and catalyses vesicle scission in a GTP-hydrolysis-dependent manner. The molecular details of oligomerization and the mechanism of the mechanochemical coupling are currently unknown. Here we present the crystal structure of human dynamin 1 in the nucleotide-free state with a four-domain architecture comprising the GTPase domain, the bundle signalling element, the stalk and the pleckstrin homology domain. Dynamin 1 oligomerized in the crystals via the stalks, which assemble in a criss-cross fashion. The stalks further interact via conserved surfaces with the pleckstrin homology domain and the bundle signalling element of the neighbouring dynamin molecule. This intricate domain interaction rationalizes a number of disease-related mutations in dynamin 2 and suggests a structural model for the mechanochemical coupling that reconciles previous models of dynamin function.

Dynamin, the founding member of the dynamin superfamily, is a 100-kDa mechanochemical enzyme (Fig. 1a) involved in the scission of clathrin-coated vesicles from the plasma membrane[1]. The brain-specific isoform dynamin 1 mediates uptake of synaptic vesicles in presynaptic terminals[2–4], whereas a function of dynamin 3 at the post-synaptic density has been described[5]. Dynamin 2 is ubiquitously expressed[6], and mutations in its middle domain (MD), pleckstrin homology (PH) domain and GTPase effector domain (GED) are linked to human diseases, for example, rare forms of centronuclear myopathy and Charcot–Marie–Tooth peripheral neuropathy[7]. Upon recruitment via the carboxy-terminal proline-rich domain (PRD), dynamin oligomerizes into helical structures around the neck of budding vesicles and catalyses vesicle scission in a GTP-hydrolysis-dependent manner[8,9]. Different mechanisms for the scission reaction have been proposed, including GTP-hydrolysis-dependent constriction[10], extension[11] and twisting[9] of the vesicle neck. Other models suggest that the GTP-bound

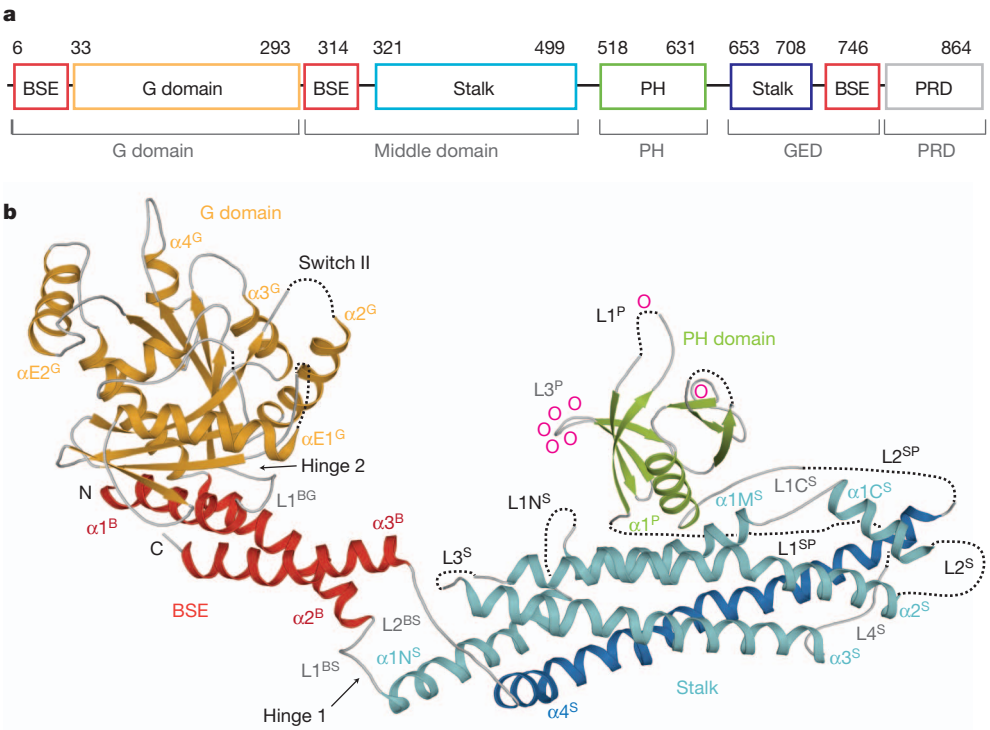

Figure 1 | Structure of nucleotide-free human dynamin 1. **a**, Structure-based domain architecture of human dynamin 1. The classical domain assignment is indicated below. **b**, Ribbon-type representation of human dynamin 1. Regions not resolved in the crystal structure are indicated by dotted lines. Domains, distinct secondary structure elements and N and C termini are labelled. Lipid-binding residues are indicated as o.

[1]Crystallography, Max-Delbrück-Centrum for Molecular Medicine, Robert-Rössle-Straße 10, 13125 Berlin, Germany. [2]Institute for Chemistry and Biochemistry, Freie Universität Berlin, Takustraße 6, 14195 Berlin, Germany. [3]Institute for Mathematics, Freie Universität Berlin, Arnimallee 6, 14195 Berlin, Germany. [4]Institute for Medical Physics and Biophysics, Charité, Ziegelstraße 5-9, 10117 Berlin, Germany. *These authors contributed equally to this work.

dynamin oligomer induces hemifusion of the inner membrane leaflet followed by complete membrane scission after GTP-hydrolysis-dependent release[12,13]. To resolve the detailed molecular mechanism, high-resolution structural data for full-length dynamin are required which, to date, are available only for the isolated PH domain[14,15] and the GTPase (G) domain[16,17]. Low-resolution electron microscopy reconstructions of dynamin oligomers showed that nucleotide binding leads to constriction of helical assemblies through rearrangements in the stalk region composed of the MD and GED[18]. Furthermore, G domain dimerization via a conserved interface across the nucleotide-binding site was shown to mediate the stimulated GTPase activity[19]. We recently described the structure of the stalk of the dynamin-like antiviral myxovirus resistance protein 1 (MxA) GTPase and elucidated its mode of oligomerization, which involves three distinct interfaces and two loop regions in the stalk[20]. Using this information, we succeeded to determine the structure of dynamin 1.

The structure of human dynamin 1

We reasoned that the propensity of dynamin to oligomerize at high protein concentrations might interfere with the formation of protein crystals. On the basis of our previous MxA study[20], we assayed a number of mutants in a human dynamin 1 construct (amino acids 6–746, Fig. 1a) for oligomerization defects. Indeed, a five-amino-acid exchange (IHGIR395–399AAAAA) in a conserved motif mapping to loop L2 of the MxA stalk[20] interfered with higher-order assembly and resulted in a monodisperse dimeric dynamin 1 species (Supplementary Fig. 1, see also ref. 21). Crystals of a construct containing additionally the K562E mutation were obtained in the absence of nucleotides and diffracted to a maximal resolution of 3.7 Å (Supplementary Table 1). The structure was solved by molecular replacement and refined to R_{work}/R_{free} of 28.4%/33.5% (Supplementary Table 1). To verify the sequence, the positions of 19 internal methionines were assigned by a single anomalous dispersion approach (Supplementary Fig. 2).

Dynamin 1(ΔPRD) has a four-domain architecture, composed of the G domain, the bundle signalling element (BSE), the stalk and the PH domain (annotated as superscript G, B, S and P, respectively), which does not strictly follow the sequence-derived domain boundaries (Fig. 1 and Supplementary Fig. 3). The structure of the amino-terminal G domain is very similar to that of the isolated nucleotide-free G domain[17] (root-mean-square deviation (r.m.s.d.) of 1.4 Å for 287 Cα atoms) and shows a curved central β-sheet surrounded by α-helices at both sides. The two switch regions known to mediate nucleotide-dependent conformational changes and the *cis* stabilizing loop, involved in G domain dimerization[19], are partly disordered. At the N and C termini of the G domain, helices $\alpha1^B$ and $\alpha2^B$, together with $\alpha3^B$ from the C-terminal part of the GED of the same molecule, form a three-helix bundle, the BSE[19,22] (Fig. 1 and Supplementary Fig. 4). Compared to the previously described G domain-BSE construct in the GDP•AlF_4^--bound form[19], $\alpha1^B$ is shifted by two turns relative to $\alpha2^B/\alpha3^B$ (Supplementary Figs 2 and 4), whereas it interacts with the G domain in a similar fashion in both structures.

At the C-terminal end of $\alpha2^B$, the BSE connects to the stalk of dynamin 1. The stalk is composed of a four-helix bundle where three helices, $\alpha1^S$–$\alpha3^S$, are provided by the MD and $\alpha4^S$ by the N-terminal part of the GED (Fig. 1 and Supplementary Fig. 5a). $\alpha1^S$ in dynamin 1 is subdivided into $\alpha1N^S$, $\alpha1M^S$ and $\alpha1C^S$ by two disordered loops, $L1N^S$ and $L1C^S$, compared to a single break of the corresponding helix in MxA. Furthermore, $\alpha3^S$ in dynamin 1 is extended by a highly conserved loop $L4^S$. At the C terminus of the stalk, $\alpha4^S$ closely packs against $\alpha1^S$–$\alpha3^S$ via hydrophobic contacts and leads the polypeptide chain back to the BSE. Despite an overall sequence identity of only 16%, the architecture of the dynamin 1 and MxA stalk is remarkably similar (r.m.s.d. of 2.6 Å for 160 aligned Cα atoms, Supplementary Fig. 5).

The PH domain is interconnected between $\alpha3^S$ and $\alpha4^S$ of the stalk by two disordered loops, $L1^{SP}$ and $L2^{SP}$, and shows only minor deviations from the isolated PH domain of dynamin 1 (refs 14, 15; r.m.s.d. of 0.8 Å for 102 Cα atoms). The three lipid binding loops[23–25] are only partially resolved and point towards the solvent (Fig. 1b and Supplementary Fig. 3).

Dynamin assembly via the stalk

Similarly to the MxA stalks[20], the dynamin 1 stalks in the crystals were arranged in a criss-cross fashion resulting in a linear stalk filament. The highly conserved symmetric interface-2 of 1,200 $Å^2$ is located in the centre of the stalk (according to the MxA nomenclature, Fig. 2 and

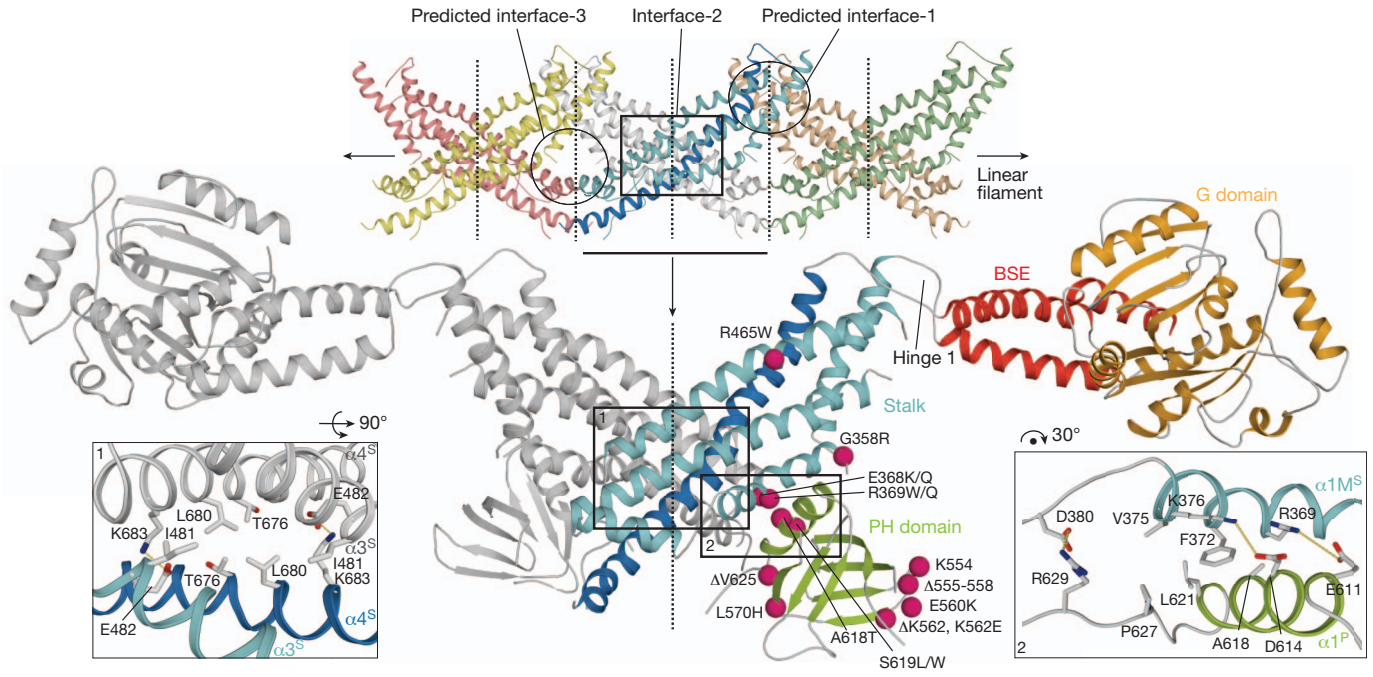

Figure 2 | The dynamin 1 dimer. In the crystals, stalks were arranged in a criss-cross fashion via crystallographic two-fold axis (black dotted lines). Assembly via the central interface-2 leads to an extended dynamin 1 dimer. Black rectangles indicate stalk interfaces shown in detail in the insets (see Supplementary Fig. 2 for PH domain assignment). Disease-related dynamin 2 mutations causing centronuclear myopathy or Charcot–Marie–Tooth[7] are represented by pink spheres, with the amino acid exchange indicated.

Supplementary Figs 3 and 5). Assembly via this interface results in an extended dynamin dimer that serves as building block for dynamin oligomers[26]. Shape and dimension of this dimer agree well with a small-angle X-ray scattering study[27].

We previously showed that a second hydrophobic interface in the MxA stalk, interface-1, mediates assembly of higher-order oligomers[20]. In dynamin 1, however, the stalks do not contact each other directly at the predicted interface-1 (minimal distance 4.5 Å, Supplementary Fig. 5). This difference is caused by a 5° tilt of the dynamin 1 stalks relative to the stalk axis. The hydrophobic nature of this surface in dynamin 1 and its conservation in the dynamin family (Supplementary Fig. 5c) is indicative of a similar function as in MxA as an oligomerization site. Closure of interface-1 might induce a pitch in the dynamin assemblies leading to helical oligomers rather than to ring-like structures as in MxA[28].

$L2^S$ containing the disruptive IHGIR395–399AAAAA mutation and $L1N^S$ are not ordered in the linear dynamin 1 oligomer (Supplementary Fig. 5). The corresponding loops in the MxA stalk form a third interface (interface-3) which also contributes to the assembly of oligomers (Fig. 2). Accordingly, mutations in both loops in dynamin 1 (ref. 21), MxA[20] and in L1 of dynamin 1-like protein[29,30] prevent oligomerization. Interestingly, Ser 347 and Tyr 354 in loop $L1N^S$ in dynamin 1 are phosphorylated *in vivo*[31,32] and might control the assembly status.

Interactions of the BSE

The BSE interacts with the central β-sheet of the G domain via a mostly hydrophilic interface of 1,100 $Å^2$ (Supplementary Figs 4 and 6). In contrast, the BSE and concomitantly the G domain are only loosely associated with the stalk of the same molecule via loops $L1^{BS}$ and $L2^{BS}$ constituting a flexible hinge (hinge 1), as observed in other dynamin related proteins[33] (Figs 1b and 2, and Supplementary Fig. 2).

Interestingly, Asp 744 at the C terminus of $\alpha3^B$ of the BSE contacts Arg 440 in $\alpha2^S$ of the neighbouring, parallel dynamin 1 stalk (Fig. 3a). A similar intermolecular interaction mediates oligomerization and the antiviral function of MxA (S.G., K.F., O.D., unpublished observation). We tested the importance of this contact experimentally. The wild-type dynamin 1 construct bound efficiently to liposomes resulting in an approximately 200-fold stimulation of GTPase activity (Supplementary Fig. 7). The single R440A and D744A mutants behaved as wild type in these assays. To analyse the role of these residues for clathrin-mediated endocytosis, dynamin 2–eGFP mutants (a fusion of dynamin 2 with enhanced green fluorescent protein) were re-expressed in HeLa cells depleted of endogenous dynamin 2. Both R440A and D744A mutants localized similarly as wild-type dynamin 2 to the plasma membrane (Supplementary Fig. 8), but transferrin internalization was increased (Fig. 3b and Supplementary Fig. 9). Thus, the salt bridge has an inhibitory and/or control function in dynamin-based endocytosis.

The stalk–PH domain interface

$\alpha1M^S$ of the stalk forms a conserved surface of 370 $Å^2$ with the PH domain (Figs 1b and 2, and Supplementary Figs 3 and 5c). Interestingly, 19 unique mutations causing centronuclear myopathy or Charcot–Marie–Tooth disease[7] cluster in the stalk or the PH domain of dynamin 2, but none localizes to the G domain or BSE (Fig. 2). For example, mutations E368K/Q and R369W/Q in the stalk and A618T and S619L/W in the PH domain are directly in or in close vicinity to the interface between the two domains. Mutations A618T and S619L/W lead to increased oligomerization rates of dynamin in solution[27,34], suggesting that the stalk–PH interface controls oligomerization. In gel filtration, the disease-related stalk mutant E368K also eluted as high molecular weight species. Consistently, this mutant showed a 20-fold increased basal GTPase rate, whereas the liposome-stimulated GTPase reaction and transferrin uptake were unchanged (Fig. 3b and Supplementary Fig. 7). In contrast, the R369W mutant behaved as wild-type dynamin in biochemical and endocytosis assays. Mutations at the periphery of

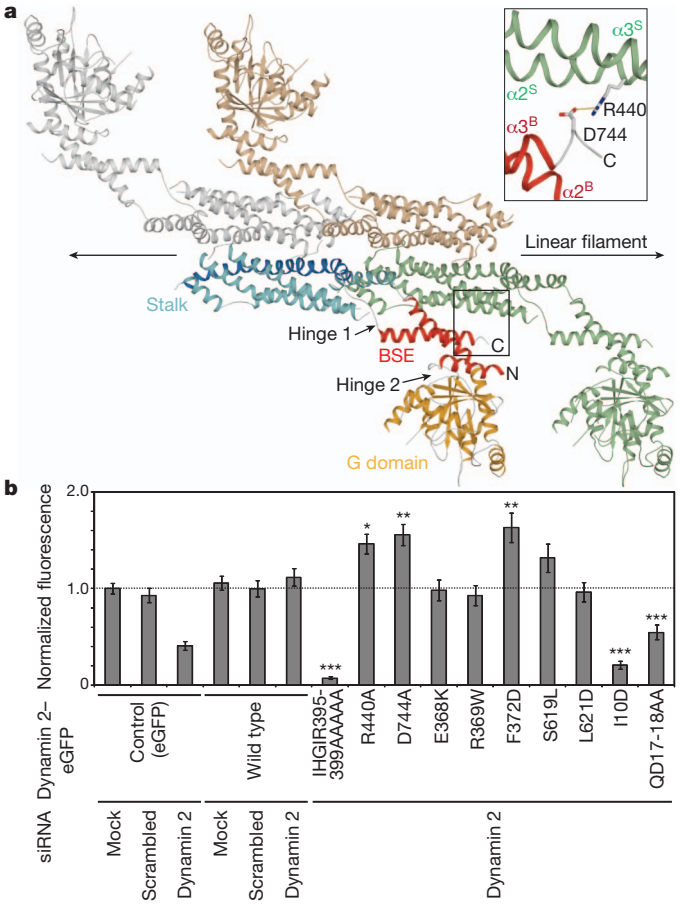

Figure 3 | Stalk interactions with the BSE and PH domain. **a**, Top view on the dynamin 1 oligomer. The PH domains are not drawn for clarity. The insert shows a close view of the intermolecular BSE–stalk interaction. **b**, HeLa cells depleted of endogenous dynamin 2 by short interfering RNA (siRNA) were transfected with a plasmid encoding siRNA-resistant dynamin 2–eGFP and allowed to endocytose fluorescently labelled transferrin. In transfected cells, fluorescence was quantified and normalized to mock-treated cells expressing eGFP. Data shown represent mean ± standard error; $*P < 0.05$; $**P < 0.01$; $***P < 0.0001$ for wild-type versus mutant dynamin 2–eGFP, as determined by *t*-test.

this interface (S619L, L621D) also did not compromise dynamin 2-based endocytic activity (Fig. 3b), indicating that more subtle changes lead to the disease-phenotype. Interestingly, the F372D mutant in the centre of the interface showed significantly higher transferrin uptake compared to wild-type dynamin 2, pointing also to an inhibitory and/or control function of this interface for dynamin-based endocytosis.

Conformational changes during dynamin assembly

Based on the isolated BSE and PH domain (Fig. 1b), the stalk dimer (Fig. 2), the GDP•AlF_4^--bound G domain dimer[19], and electron microscopy reconstructions of oligomerized dynamin 1 in the constricted state[18], we generated a molecular model for self-assembly of dynamin into helical structures (Fig. 4a and Supplementary Fig. 10). The resulting dynamin dimer spans a length of more than 260 Å and covers 95° of a dynamin ring, thereby placing G domain and BSE above the neighbouring stalk. According to this model, oligomerization of dynamin proceeds along the central stalk, whereas the G domains mediate contacts between neighbouring turns (see ref. 20 for a similar MxA model).

When comparing the linear structure of dynamin 1 in the crystal with the helical assembly, large-scale domain movements are apparent (Supplementary Fig. 11). The G domain-BSE unit is shifted and rotated

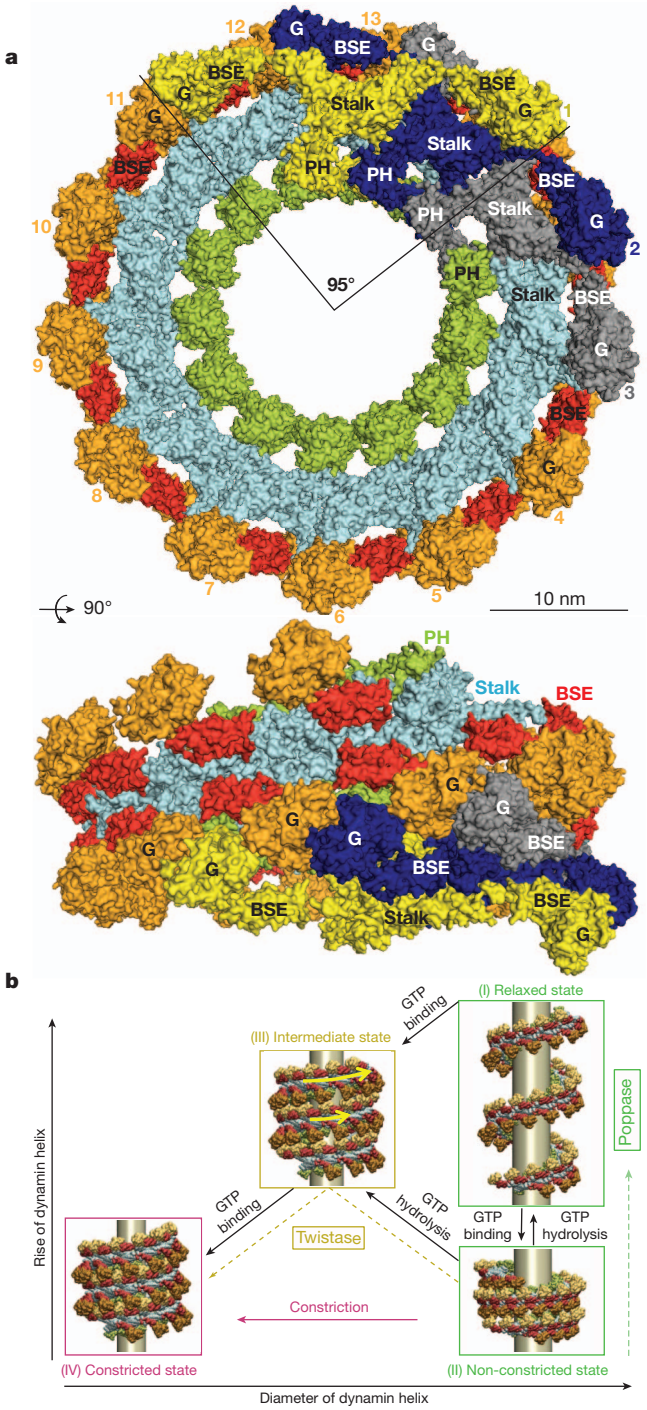

Figure 4 | Model for dynamin oligomerization and function. **a**, Model of the oligomerized dynamin helix in the constricted state, in top and side view (see also Supplementary Fig. 10). Three dimers (1–3) are uniformly coloured. Whereas 13 stalk dimers complete one turn, the G domain of dimer (*i*) associates with the G domain of dimer (*i* + 10). **b**, Structure-based illustration for the proposed mechanism of the dynamin oligomer. Variations in the assembly of consecutive dynamin molecules lead to dynamin helices of different rise and diameter. For further explanation, see main text and Supplementary Fig. 12.

around hinge 1 upon oligomerization. Additionally, the G domain separates from the BSE by a rotation around the invariant Pro 32 and Pro 294 (Supplementary Fig. 6). The corresponding residues Gly 68 and Gly 309 in BDLP[33,35] and Pro 342 in atlastin[36,37] have also been suggested to act as a hinge (hinge 2). Integrity of the G domain–BSE interface is crucial for the function of dynamin, as indicated by the aggregation of the I10D interface mutant *in vivo* (Supplementary Figs 6 and 8). Furthermore, I10D behaved as a dominant-negative mutant in transferrin uptake assays (Fig. 3b). Moreover, the QD17–18AA mutation rendered dynamin 2 largely inactive in endocytosis assays, despite localizing correctly to clathrin-coated pits at the plasma membrane (Fig. 3b and Supplementary Fig. 8).

The PH domains also undergo a pronounced rearrangement, to a position below the stalk, with the lipid-binding loops[23–25] oriented towards the membrane (Supplementary Fig. 11a). We suggest that the stalk PH domain interface is disrupted by binding of the PH domain to high-affinity, phosphatidylinositol-4,5-bisphosphate-containing membranes such as the plasma membrane[23–25], thereby promoting dynamin oligomerization.

Finally, we suggest that rotation of stalk dimers via the flexible interface-1 and/or interface-3, leaving interface-2 unchanged, leads to bending of the linear oligomer and allows helix formation (Supplementary Figs 11b and 12). Interestingly, the IHGIR395–399AAAAA mutation in interface-3 prevented liposome binding and, consequently, the liposome-stimulated GTPase activity (Supplementary Fig. 7). This mutant further behaved in a dominant-negative fashion in transferrin uptake assays (Fig. 3b) and displayed a diffuse localization and reduced recruitment to clathrin-coated pits (Supplementary Fig. 8). These results point to the central role of interface-3 for the function of dynamin.

Discussion

The present work, combined with prior studies[18–20,38], suggests a structural model for the mechanochemical coupling in dynamin that is consistent with previous models[9–11]. Our structural analysis indicates that the diameter of helical dynamin assemblies is controlled by the angle between two stalk dimers (Supplementary Figs 11b and 12f–h). We suggest that this angle is adjusted in response to GTP-dependent dimerization of the G domains: a relaxed conformation of interface-1 is adopted in the absence of G domain constraints, whereas GTP-triggered dimerization of the G domains constrains rotation in interface-1 and induces a bent, constricted conformation (Supplementary Fig. 11b), possibly via the BSE–stalk interface (Fig. 3a). Interestingly, in molecular dynamics simulations of two stalk dimers, the bent conformation of interface-1 rapidly converts towards a relaxed state, concomitant with an opening of the helical oligomer (Fig. 4b and Supplementary Fig. 12). This supports our assumption that constraints from G domains dimerization are required for the stabilization of the constricted state.

Accordingly, dynamin initially assembles via the stalks with interface-1 in a relaxed conformation, allowing the filament to adopt a range of different diameters[12] (state I in Fig. 4b and Supplementary Fig. 12). When the filament has embraced its template, GTP-loaded G domains of adjacent turns dimerize, the inhibitory stalk–BSE interface (Fig. 3a) is disrupted and the bent conformation of interface-1 is induced. This will result in constriction of the filament if the lipid template is flexible (state IV in Fig. 4b, constrictase model[10]) or compaction of the dynamin helix if the lipid template is rigid (state II in Fig. 4b, poppase model[11]). Constriction of a long dynamin helix will induce a sliding of neighbouring filaments until a new constricted equilibrium position of the oligomer is reached. This sliding is observed as a rotary movement of the dynamin helix upon addition of GTP in real-time imaging assays (twistase model[9]). To reach the constricted state along the whole assembly, several cycles of local release and rebinding of neighbouring dynamin turns might be triggered by GTP-dependent dimerization of G domains and dissociation after GTP hydrolysis (state III in Fig. 4b). Accordingly, GTP binding and hydrolysis are both required for the mechanochemical function of dynamin[8,39] and might induce local opening or twisting of the constricted dynamin helix. The resulting shear forces could tear the underlying membrane.

The complex domain interplay in dynamin rationalizes the high degree of structural conservation in the dynamin superfamily, sheds light on the molecular mechanisms of disease-associated mutations and highlights structural features of the nucleotide-free state as a prerequisite to understand dynamin's mechanochemical function.

METHODS SUMMARY

A human dynamin 1 construct (residues 6–746) containing the IHGIR395–399AAAAA and K562E mutations was expressed as a His_6-tag-fusion in *Escherichia coli* and purified to homogeneity. Crystals were obtained using PEG400 and isopropanol as precipitants. The structure was solved by molecular replacement. To verify the model, the positions of 19 out of 26 methionines were determined by an anomalous data set of SeMet-substituted crystals. Liposome binding assays were carried out as described (http://www.endocytosis.org). GTPase assays were carried out at 37 °C using 20 mM HEPES/NaOH, pH 7.5, 150 mM NaCl, 2 mM KCl, 2 mM $MgCl_2$ as reaction buffer. Uptake of fluorescently labelled transferrin was monitored in HeLa cells depleted of endogenous dynamin 2 by siRNA and transfected with the indicated siRNA-resistant dynamin 2 constructs.

Full Methods and any associated references are available in the online version of the paper at www.nature.com/nature.

Received 8 March; accepted 17 July 2011.
Published online 18 September 2011.

1. Praefcke, G. J. & McMahon, H. T. The dynamin superfamily: universal membrane tubulation and fission molecules? *Nature Rev. Mol. Cell Biol.* **5,** 133–147 (2004).
2. van der Bliek, A. M. & Meyerowitz, E. M. Dynamin-like protein encoded by the *Drosophila shibire* gene associated with vesicular traffic. *Nature* **351,** 411–414 (1991).
3. Ferguson, S. M. *et al.* A selective activity-dependent requirement for dynamin 1 in synaptic vesicle endocytosis. *Science* **316,** 570–574 (2007).
4. Robinson, P. J. *et al.* Dynamin GTPase regulated by protein kinase C phosphorylation in nerve terminals. *Nature* **365,** 163–166 (1993).
5. Lu, J. *et al.* Postsynaptic positioning of endocytic zones and AMPA receptor cycling by physical coupling of dynamin-3 to Homer. *Neuron* **55,** 874–889 (2007).
6. Cook, T. A., Urrutia, R. & McNiven, M. A. Identification of dynamin 2, an isoform ubiquitously expressed in rat tissues. *Proc. Natl Acad. Sci. USA* **91,** 644–648 (1994).
7. Durieux, A. C. *et al.* Dynamin 2 and human diseases. *J. Mol. Med.* **88,** 339–350 (2010).
8. Marks, B. *et al.* GTPase activity of dynamin and resulting conformation change are essential for endocytosis. *Nature* **410,** 231–235 (2001).
9. Roux, A. *et al.* GTP-dependent twisting of dynamin implicates constriction and tension in membrane fission. *Nature* **441,** 528–531 (2006).
10. Hinshaw, J. E. & Schmid, S. L. Dynamin self-assembles into rings suggesting a mechanism for coated vesicle budding. *Nature* **374,** 190–192 (1995).
11. Stowell, M. H. B. *et al.* Nucleotide-dependent conformational changes in dynamin: evidence for a mechanochemical molecular spring. *Nature Cell Biol.* **1,** 27–32 (1999).
12. Bashkirov, P. V. *et al.* GTPase cycle of dynamin is coupled to membrane squeeze and release, leading to spontaneous fission. *Cell* **135,** 1276–1286 (2008).
13. Pucadyil, T. J. & Schmid, S. L. Real-time visualization of dynamin-catalyzed membrane fission and vesicle release. *Cell* **135,** 1263–1275 (2008).
14. Timm, D. *et al.* Crystal structure of the pleckstrin homology domain from dynamin. *Nature Struct. Biol.* **1,** 782–788 (1994).
15. Ferguson, K. M. *et al.* Crystal structure at 2.2 Å resolution of the pleckstrin homology domain from human dynamin. *Cell* **79,** 199–209 (1994).
16. Niemann, H. H. *et al.* Crystal structure of a dynamin GTPase domain in both nucleotide-free and GDP-bound forms. *EMBO J.* **20,** 5813–5821 (2001).
17. Reubold, T. F. *et al.* Crystal structure of the GTPase domain of rat dynamin 1. *Proc. Natl Acad. Sci. USA* **102,** 13093–13098 (2005).
18. Mears, J. A., Ray, P. & Hinshaw, J. E. A corkscrew model for dynamin constriction. *Structure* **15,** 1190–1202 (2007).
19. Chappie, J. S. *et al.* G domain dimerization controls dynamin's assembly-stimulated GTPase activity. *Nature* **465,** 435–440 (2010).
20. Gao, S. *et al.* Structural basis of oligomerization in the stalk region of dynamin-like MxA. *Nature* **465,** 502–506 (2010).
21. Ramachandran, R. *et al.* The dynamin middle domain is critical for tetramerization and higher-order self-assembly. *EMBO J.* **26,** 559–566 (2007).
22. Chappie, J. S. *et al.* An intramolecular signaling element that modulates dynamin function *in vitro* and *in vivo*. *Mol. Biol. Cell* **20,** 3561–3571 (2009).
23. Vallis, Y. *et al.* Importance of the pleckstrin homology domain of dynamin in clathrin-mediated endocytosis. *Curr. Biol.* **9,** 257–263 (1999).
24. Zheng, J. *et al.* Identification of the binding site for acidic phospholipids on the pH domain of dynamin: implications for stimulation of GTPase activity. *J. Mol. Biol.* **255,** 14–21 (1996).
25. Salim, K. *et al.* Distinct specificity in the recognition of phosphoinositides by the pleckstrin homology domains of dynamin and Bruton's tyrosine kinase. *EMBO J.* **15,** 6241–6250 (1996).
26. Zhang, P. & Hinshaw, J. E. Three-dimensional reconstruction of dynamin in the constricted state. *Nature Cell Biol.* **3,** 922–926 (2001).
27. Kenniston, J. A. & Lemmon, M. A. Dynamin GTPase regulation is altered by PH domain mutations found in centronuclear myopathy patients. *EMBO J.* **29,** 3054–3067 (2010).
28. Kochs, G. *et al.* Assay and functional analysis of dynamin-like Mx proteins. *Methods Enzymol.* **404,** 632–643 (2005).
29. Ingerman, E. *et al.* Dnm1 forms spirals that are structurally tailored to fit mitochondria. *J. Cell Biol.* **170,** 1021–1027 (2005).
30. Chang, C. R. *et al.* A lethal *de novo* mutation in the middle domain of the dynamin-related GTPase Drp1 impairs higher order assembly and mitochondrial division. *J. Biol. Chem.* **285,** 32494–32503 (2010).
31. Graham, M. E. *et al.* The *in vivo* phosphorylation sites of rat brain dynamin I. *J. Biol. Chem.* **282,** 14695–14707 (2007).
32. Rush, J. *et al.* Immunoaffinity profiling of tyrosine phosphorylation in cancer cells. *Nature Biotechnol.* **23,** 94–101 (2004).
33. Low, H. H. & Lowe, J. Dynamin architecture–from monomer to polymer. *Curr. Opin. Struct. Biol.* **20,** 791–798 (2010).
34. Wang, L. *et al.* Dynamin 2 mutants linked to centronuclear myopathies form abnormally stable polymers. *J. Biol. Chem.* **285,** 22753–22757 (2010).
35. Low, H. H. *et al.* Structure of a bacterial dynamin-like protein lipid tube provides a mechanism for assembly and membrane curving. *Cell* **139,** 1342–1352 (2009).
36. Byrnes, L. J. & Sondermann, H. Structural basis for the nucleotide-dependent dimerization of the large G protein atlastin-1/SPG3A. *Proc. Natl Acad. Sci. USA* 10.1073/pnas.1012792108 (10 January 2011).
37. Bian, X. *et al.* Structures of the atlastin GTPase provide insight into homotypic fusion of endoplasmic reticulum membranes. *Proc. Natl Acad. Sci. USA* **108,** 3976–3981 (2011).
38. Klockow, B. *et al.* The dynamin A ring complex: molecular organization and nucleotide-dependent conformational changes. *EMBO J.* **21,** 240–250 (2002).
39. Morlot, S. *et al.* Deformation of dynamin helices damped by membrane friction. *Biophys. J.* **99,** 3580–3588 (2010).

Supplementary Information is linked to the online version of the paper at www.nature.com/nature.

Acknowledgements This project was supported by a grant from the Deutsche Forschungsgemeinschaft (SFB 740/C7 and SFB958/A12 to O.D., SFB740/D7 and SFB958/A04 to F.N., SFB740/C8 and SFB 958/A7 to V.H.), by a Career Development Fellowship of The International Human Frontier Science Program Organization and by the EMBO Young Investigator Program to O.D. We would like to thank S. Werner, M. Papst and S. Kraft for technical assistance, the BESSY staff at BL14.1 for help during data collection, G. Schröder for advice in DEN refinement and U. Heinemann for discussions.

Author Contributions K.F., Y.P., D.S. and Y.R. performed experiments, K.F., Y.P., S.G., M.H., V.H., F.N. and O.D. designed research, M.H. and. F.N. conducted and analysed molecular modelling and molecular dynamics simulations. K.F. and O.D. wrote the manuscript.

Author Information The atomic coordinates of human dynamin 1 have been deposited in the Protein Data Bank with accession number 3SNH. Reprints and permissions information is available at www.nature.com/reprints. The authors declare no competing financial interests. Readers are welcome to comment on the online version of this article at www.nature.com/nature. Correspondence and requests for materials should be addressed to O.D. (oliver.daumke@mdc-berlin.de) or K.F. (katja.faelber@mdc-berlin.de).

METHODS

Protein expression and purification. Human dynamin 1 (residues 6–746) and indicated mutants of this construct were expressed from pET46-EK/LIC (Novagen) as N-terminal His_6-tag fusion followed by a PreScission cleavage site. The crystallized construct contained mutations IHGIR395–399AAAAA which prevented oligomerization and K562E which reduced DNA contaminations during purification. Proteins were expressed in *Escherichia coli* host strain Rosetta2-BL21-DE3, and bacteria were cultured in autoinduction medium (Novagen) for 7.5 h at 37 °C followed by temperature shift to 20 °C for overnight expression. Selenomethionine (SeMet)-substituted human dynamin 1 was expressed in M9 minimal medium, supplemented with L-amino acids Lys, Phe, Thr (100 mg l^{-1}), Ile, Leu, Val, SeMet (50 mg l^{-1}), using the same vector and host strain as for native protein expression[40]. Cells were resuspended in buffer A (25 mM HEPES/NaOH (pH 7.9), 500 mM NaCl, 2 mM $MgCl_2$, 1 µM DNase (Roche), 500 µM Pefabloc (Roth)) and disrupted by a microfluidizer (Microfluidics). Cleared lysates (95,000*g*, 1 h, 4 °C) were incubated with Benzonase (Novagen) for 30 min at 4 °C before application to a Co^{2+}-Talon column (Clontech). Protein was eluted with buffer A containing additional 100 mM imidazole. Fractions containing human dynamin 1 were incubated with 2.4 mM β-mercaptoethanol and His_6-tagged Prescission protease overnight at 4 °C. Using 50 kDa molecular weight cut-off concentrators (Amicon), imidazole, β-mercaptoethanol and the free His-tag were removed by washing with buffer A, before a second application to a Co^{2+}-Talon column to remove non-cleaved His-tagged dynamin 1 and protease. The flow-through and four column volumes of washing buffer A were collected and concentrated. Finally, dynamin 1 was purified by size exclusion chromatography on a Superdex200 column (GE) in buffer containing 25 mM HEPES/NaOH (pH 7.5), 300 mM NaCl, 2 mM $MgCl_2$. Fractions containing dynamin 1 were pooled, concentrated and flash-frozen in liquid nitrogen (Supplementary Fig. 1). SeMet-substituted protein was purified using the same protocol.

Crystallization and structure determination. Crystallization trials by the sitting-drop vapour-diffusion method were performed at 4 °C using a Hydra-plus-One pipetting robot (Matrix Technologies Corporation) and Rock Imager storage system (Formulatrix). The human dynamin 1 construct (300 nl at a concentration of 12 mg ml^{-1}) was mixed with an equal volume of reservoir solution containing 9% PEG400, 6% isopropanol, 100 mM HEPES/NaOH (pH 7.3), 10 mM $MgCl_2$ and 10 mM KCl. Crystals of the native protein appeared after 2 weeks and had dimensions of 0.2 mm × 0.05 mm × 0.02 mm. Crystals of SeMet protein were obtained in 6% MPD, 10% isopropanol, 0.1 M HEPES/NaOH (pH 7.5). During flash-cooling of the crystals in liquid nitrogen, a cryo-solution containing additionally 20% ethylene glycol was used. All data were recorded at BL14.1 at BESSY II, Berlin. One native data set was collected from a single crystal and processed and scaled using the XDS program suite[41]. Phase information was obtained by molecular replacement with Phaser[42] using the structure of the nucleotide-free rat dynamin 1 G domain[16], the stalk of human MxA[20] and the human PH domain[15] as search models. The model was built using COOT[43] and iteratively refined using CNS1.3 with a deformable elastic network[44], followed by 10 cycles of TLS refinement using 1 TLS group per domain in refmac5 (ref. 45). To confirm the amino acid sequence, a data set of a SeMet-substituted protein crystal was recorded at the selenium peak wavelength. Owing to non-isomorphism of the native and SeMet crystals, molecular replacement with the refined native structure was performed. The positions of 19 out of 26 selenium atoms in the dynamin 1 construct were determined by calculating an anomalous difference map with the CCP4 program suite[46] using the calculated phases after refinement. The final native model comprises amino acids 6–746. Residues 63–64, 110–112, 143–149, 347–356, 394–404, 446–447, 500–517, 534–537, 578–581 and 632–652 are disordered. Electron density for loop $L2^{BS}$ (amino acids 709––715) was only visible in the SeMet derivative structure and was therefore not modelled in the native structure. However, $L2^{BS}$ was included for figure preparation. Of all residues, 86.9% are in the most favoured regions of the Ramachandran plot and no residue in the disallowed regions, as analysed with Procheck[47]. Figures were prepared with PyMol[48]. Buried surface areas (per molecule) were calculated using CNS[44]. Solvent-accessible areas per residue were calculated using areaimol[46]. Domain superpositions were performed with lsqkab[46]. Sequences were aligned using CLUSTAL W[49] and adjusted by hand.

Liposome co-sedimentation assays. Liposomes were prepared as previously described (http://www.endocytosis.org). Folch liposomes (total bovine brain lipids fraction I from Sigma) in 20 mM HEPES/NaOH (pH 7.5), 150 mM NaCl, 2 mM KCl were extruded through a 0.1 µm filter. Liposomes (0.1 mg ml^{-1}) were incubated at room temperature with 4.0 µM of the indicated dynamin 1 construct for 10 min in 40 µl reaction volume, followed by a 70,000*g* spin for 10 min at 20 °C.

GTP hydrolysis assay. GTPase activities of 1 µM of the indicated dynamin 1 constructs were determined at 37 °C in 20 mM HEPES/NaOH (pH 7.5), 150 mM NaCl, 2 mM KCl, 2 mM $MgCl_2$, in the absence and presence of 0.1 mg ml^{-1} 0.1-µm-filtered Folch liposomes, using saturating concentrations of GTP as substrate (1 mM for the basal and 3 mM for the stimulated reactions). Reactions were initiated by the addition of protein to the reaction. At different time points, reaction aliquots were diluted 15-fold in GTPase buffer and quickly transferred to liquid nitrogen. Nucleotides in the samples were separated via a reversed-phase Hypersil ODS-2 C18 column (250 × 4 mm), with 10 mM tetrabutylammonium bromide, 100 mM potassium phosphate (pH 6.5), 7.5% acetonitrile as running buffer. Denatured proteins were adsorbed at a C18 guard column. Nucleotides were detected by absorption at 254 nm and quantified by integration of the corresponding peaks. Rates were derived from a linear fit to the initial reaction (<40% GTP hydrolysed).

Transferrin uptake in HeLa cells. HeLa cells were transfected with siRNA using Oligofectamine (Invitrogen) on day 1. The sequence of the siRNA against human dynamin 2 is 5′-GCAACUGACCAACCACAUC-3′, targeting nucleotides 849–867. On day 2, cells were transfected with pEGFP-N1 (Clontech) or siRNA-resistant rat dynamin 2-pEGFP-N1 using lipofectamine 2000 (Invitrogen) and seeded on coverslips. On day 3, cells were serum-starved and incubated with 20 µg ml^{-1} transferrin-Alexa568 (Molecular Probes, Invitrogen) for 10 min at 37 °C. After four PBS washes on ice, cells were paraformaldehyde-fixed for 20 min at room temperature. Transferrin uptake was analysed using a Zeiss Axiovert200M microscope and Slidebook imaging software (3i Inc.). Internalized transferrin was quantified from transfected cells only and normalized to the value of eGFP-transfected, mock-treated cells ($n = 28$–83 images, five independent experiments; IHGVR395–399AAA, I10D, QD17–18AA: three independent experiments; E368K, R369W, S619L, F372D: two independent experiments). Knockdown of dynamin 2 and expression levels of dynamin 2–eGFP mutants were assessed by immunoblotting using antibodies to dynamin 2 (a gift of M. A. McNiven), β-actin (clone ac-15, Sigma-Aldrich) and eGFP (clone jl-8, Clontech).

Localization of dynamin 2–eGFP mutants. HeLa cells were transfected with dynamin 2-pEGFP-N1 wild-type or mutant constructs 20 h before fixation in 4% paraformaldehyde for 12 min at room temperature. Cells were blocked and permeabilized in 10% goat serum, 0.3% Triton X-100, 100 mM NaCl in phosphate buffer and stained for endogenous adaptor complex AP-2 using an antibody to α-adaptin (clone AP-6, Abcam). Total internal reflection fluorescence (TIRF) imaging was performed using a Zeiss Axiovert200M microscope equipped with a ×100 TIRF objective and a dual-colour TIRF setup from Visitron Systems using Slidebook imaging software (3i Inc.).

Loop modelling and molecular dynamics simulations. For modelling of the unresolved loop regions $L1N^S$ and $L2^S$, two stalk dimers in the constricted state served as scaffold. Using Modeller (9v8)[50], the scaffold was fixed in position, whereas $L1N^S$ and $L2^S$ could freely sample the empirical potential function. To reduce the conformational search space, additional harmonic distance restraints were added between conserved residues Arg 399–Asp 406 and Glu 355–Arg 361. Based on the modelled stalk tetramer, five independent all-atom molecular dynamics simulations (NVT ensemble), each of 90 ns, were conducted at $T = 300$ K in a periodic boundary setting using Gromacs 4.5.3 (ref. 51). The model was immersed in a rectangular 20 nm × 10 nm × 9 nm box, containing approximately 56,400 water molecules, 21 sodium and 17 chloride ions to neutralize the system, resulting in a total number of 185,857 atoms. As force fields, Amber99 (protein and ions)[52] and TIP3P (water)[53] were applied. To treat long-range interactions, the Particle-mesh Ewald method[54,55] was used. A cut-off of 1 nm was used for the real parts of electrostatic and van der Waals interactions. All hydrogen bonds were constrained by using the LINCS[56] algorithm, allowing for an integration time-step of 2 fs. For the thermostatted integration, Langevin dynamics were used as implemented by the Gromacs s.d. integrator (tau_t = 1).

For the calculation of bending and twisting angles, each of the four stalk monomers was represented by two geometric centres, defined as the mean position of Cα atoms of residues 366–377, 420–430, 468–481 and 671–683 for position A and residues 360–365, 428–445, 457–472 and 686–701 for position B (Supplementary Fig. 12d). The stalk bending angle α was defined as the mean angle between parallel stalks, and the twisting angle β by the minimal angle between the planes spanned by each dimer (positions A, B, B′ in Supplementary Fig. 12f).

For each simulation time step, the corresponding stalk tetramer structure describes a linear transformation of the first dimer onto the second dimer, consisting of a translation vector and a rotation matrix. This linear transformation was used to reconstruct the structure of an ideal dynamin helix by applying it to the dynamin dimer model in the constricted state. The diameter, d, and the rise per turn, r, of these helices were measured by using the geometric centres of the stalk coordinates and obtaining trajectories in (d,r). Based on these trajectories, the free energy surface of stalk helix conformations was calculated: the two-dimensional space (d,r) was discretized into boxes of size 25 × 25 Å. Based on the simulation trajectories, the transition probability between all pairs of boxes was computed,

which allowed the calculation of an equilibrium probability of finding a single stalk tetramer in a given box, $p_1(d,r)$[57]. When more than two stalk dimers are assembled, non-cooperative behaviour of neighbouring dimers has to be considered, for example, the assembled stalk dimers can almost independently switch between different conformations. The resulting equilibrium distribution of two independent tetrameric units would be given by the convolution of two single-tetramer distributions, $p_2(d,r)$. It was found that for only about three such convolutions, the resulting probability distribution converges to $p_3(d,r) \approx p(d,r)$. Thus, assuming that the helix has at least three independently switching subunits, the free energy landscape is unique, and is given by $F(d,r) = -\mathrm{k}T\ln(p(d,r))$, where k is the Boltzmann constant and T the temperature.

40. Van Duyne, G. D. *et al.* Atomic structures of the human immunophilin FKBP-12 complexes with FK506 and rapamycin. *J. Mol. Biol.* **229,** 105–124 (1993).
41. Kabsch, W. Automatic processing of rotation diffraction data from crystals of initially unknown symmetry and cell constants. *J. Appl. Cryst.* **26,** 795–800 (1993).
42. McCoy, A. J. *et al. Phaser* crystallographic software. *J. Appl. Cryst.* **40,** 658–674 (2007).
43. Emsley, P. & Cowtan, K. *Coot*: model-building tools for molecular graphics. *Acta Crystallogr. D* **60,** 2126–2132 (2004).
44. Schröder, G. F., Levitt, M. & Brunger, A. T. Super-resolution biomolecular crystallography with low-resolution data. *Nature* **464,** 1218–1222 (2010).
45. Murshudov, G. N., Vagin, A. A. & Dodson, E. J. Refinement of macromolecular structures by the maximum-likelihood method. *Acta Crystallogr. D* **53,** 240–255 (1997).
46. Collaborative Computational Project, Number 4. The *CCP4* suite: programs for protein crystallography. *Acta Crystallogr. D* **50,** 760–763 (1994).
47. Laskowski, R. A. *et al.* PROCHECK: a program to check the stereochemical quality of protein structures. *J. Appl. Cryst.* **26,** 283–291 (1993).
48. DeLano, W. L. *The PyMol Molecular Graphics System* version 1.4.1 (Schrödinger, 2011).
49. Thompson, J. D., Higgins, D. G. & Gibson, T. J. CLUSTAL W: improving the sensitivity of progressive multiple sequence alignment through sequence weighting, position-specific gap penalties and weight matrix choice. *Nucleic Acids Res.* **22,** 4673–4680 (1994).
50. Fiser, A., Do, R. K. & Sali, A. Modeling of loops in protein structures. *Protein Sci.* **9,** 1753–1773 (2000).
51. Van Der Spoel, D. *et al.* GROMACS: fast, flexible, and free. *J. Comput. Chem.* **26,** 1701–1718 (2005).
52. Wang, J. M., Cieplak, P. & Kollman, P. A. How well does a restrained electrostatic potential (RESP) model perform in calculating conformational energies of organic and biological molecules? *J. Comput. Chem.* **21,** 1049–1074 (2000).
53. Jorgensen, W. *et al.* Comparison of simple potential functions for simulating liquid water. *J. Chem. Phys.* **79,** 926–935 (1983).
54. Essmann, U. *et al.* A smooth particle mesh Ewald method. *J. Chem. Phys.* **103,** 8577–8593 (1995).
55. Darden, T., York, D. & Pedersen, L. Particle mesh Ewald: an $N\cdot\log(N)$ method for Ewald sums in large systems. *J. Chem. Phys.* **98,** 10089–10092 (1993).
56. Hess, B. *et al.* LINCS: a linear constraint solver for molecular simulations. *J. Comput. Chem.* **18,** 1463–1472 (1997).
57. Prinz, J. H. *et al.* Markov models of molecular kinetics: generation and validation. *J. Chem. Phys.* **134,** 174105 (2011).